Castro, V. de, Lozano Pérez, S., Briceno, M., Trocellier, P., Roberts, S. G., Pareja, R. (2015). Effects of single- and simultaneous triple-ion-beam irradiation on an oxide dispersion-strengthened Fe12Cr steel. *Journal of Materials Science*, 50, pp. 2306–2317.

DOI: https://doi.org/10.1007/s10853-014-8794-y

J Mater Sci
DOI 10.1007/s10853-014-8794-y

Effects of single- and simultaneous triple-ion-beam irradiation on an oxide dispersion-strengthened Fe12Cr steel

Vanessa de Castro · Sergio Lozano-Perez · Martha Briceno · Patrick Trocellier · Steve G. Roberts · Ramiro Pareja

Received: 7 August 2014 / Accepted: 15 December 2014

Abstract Oxide dispersion-strengthened (ODS) steels are main candidates for structural applications in future fusion reactors. Understanding their irradiation-induced behaviour is a key in building optimised components with enhanced radiation resistance. In this work, the stability of an ODS Fe12Cr steel was investigated by transmission electron microscopy after single- (Fe^{4+}) and simultaneous triple-ion-beam irradiation (Fe^{8+}, He^{+} and H^{+}) at room temperature to doses of 4.4 and 10 dpa. The irradiations were accomplished at the JANNUS-Saclay facility. Results after single-ion-beam irradiation were also compared with those from a reference Fe12Cr steel produced following the same route. Analyses focused on determining the irradiation-induced loop size and density in the ODS and reference materials, investigating the grain boundary microchemistry and studying the evolution of the secondary phases present. These experiments show that the Y-rich nanoparticles present in the ODS steel are quite stable under these irradiation conditions although evolution of larger Cr-rich carbides could be taking place. Loop sizes are smaller for the ODS steel than for the reference material and appear to increase with dose. Cr segregates at some of the grain boundaries, though this segregation also occurs in the absence of irradiation.

V. de Castro (✉) · R. Pareja
Departamento de Física, Universidad Carlos III de Madrid, Avda. de la Universidad 30, 28911 Leganés, Madrid, Spain
e-mail: vanessa.decastro@uc3m.es

S. Lozano-Perez · M. Briceno · S. G. Roberts
Department of Materials, University of Oxford, Oxford OX1 3PH, UK

M. Briceno
Johnson Matthey Technology Centre, Blount's Court Rd, Sonning Common RG4 9NH, UK

P. Trocellier
CEA, DEN, Service de Recherches de Métallurgie Physique, Laboratoire JANNUS, 91191 Gif-sur-Yvette, France

S. G. Roberts
Culham Centre for Fusion Energy, Culham Science Centre, Abingdon OX14 3DB, UK

Introduction

In the roadmap for achieving viable fusion power reactors, research on the materials required to build safe and efficient reactors is of prime importance. The structure of the blanket and first wall of fusion reactors will be largely made of steel. Steels for these applications will work at high temperatures (up to possibly 550 °C [1]) and will have to withstand the radiation damage from the 14 MeV neutrons resulting from the fusion reactions. These demanding requirements must be fulfilled by reduced activation (RA) steels with enhanced capabilities. RA oxide dispersion-strengthened (ODS) ferritic-martensitic (FM) and ferritic steels with Cr contents ~9–15 wt% are prime candidates for these applications [1]. In order to obtain the desired oxide nanoparticle strengthening, these steels are produced by powder metallurgy routes usually involving mechanical alloying (MA) and consolidation by hot isostatic pressing (HIP) or hot extrusion. The consolidated material is then subjected to thermomechanical treatments to optimise its mechanical performance. These fabrication routes result in complex microstructures (sub-micron grain sizes, large amount of dislocations, high densities of Y-rich nano-sized oxide phases) that aid creep strength and enhance grain refinement, and which are thought to provide a high concentration of sinks for irradiation-induced defects and

Journal : Large 10853 Dispatch : 18-12-2014 Pages : 12
Article No. : 8794 ☐ LE ☐ TYPESET
MS Code : JMSC-D-14-03261 ☑ CP

transmutation gases, improving radiation resistance significantly as compared to their non-ODS counterparts [2, 3].

The stability of the Y-rich nanoparticles is key to achieve an optimal performance of the material during service in a fusion reactor. In principle, it is supposed that nanoparticles would be thermally stable. However, dissolution of Y–Ti oxides has been recently reported while heating above 600 °C [4]. Under irradiation, it has been found that the oxide dispersion in ODS (9–19 wt% Cr) steels is apparently unaltered after H^+ irradiation at 350 °C and 1 displacement per atom (dpa), and after simultaneous dual irradiation with Fe and He ions at 500 °C and 20 dpa [5–7]. However, amorphization of the dispersion particles was reported for an ODS Eurofer steel H^+ irradiated at room temperature (RT) to 2 dpa [8]. Nanoparticles present in a model Fe–Y_2O_3 alloy were stable after Fe ion irradiation to 100 dpa and 500 °C but significant evolution was found after dual irradiation at 600 °C to 100 dpa and 360 ppm He [9]. Investigations into the dispersion stability in irradiated ODS steels containing ~0.2–2.2 wt % Ti, where an Y–Ti–O nanoparticle dispersion is formed, have been recently summarised in Ref. [10]. In the case of ion irradiations, most studies report that oxide nanoparticles remain stable after irradiation to doses between 0.7 and 200 dpa at temperatures in the range 300–650 °C [10, 11]. However, results in 9Cr ODS steels irradiated with Ni ions at 500, 600 and 700 °C and doses of 5, 50 and 150 dpa indicate that sizes of the oxide dispersoids decrease with increasing dose and temperature [12]. Moreover, a Ni^{2+} irradiation at −75 °C to 100 dpa in the ODS alloy Fe–14Cr–3W–0.4Ti–0.25Y_2O_3 (wt%) (14YWT) resulted in complete dissolution of the nanodispersoids [13]. For neutron irradiations, no significant changes were found in the nanoparticles present in ODS steels containing ~9–12 wt% Cr and 0.2–0.3 wt% Ti when irradiated at 15 dpa in the temperature range 330–500 °C [14]. In contrast, an evolution of the nanoparticles is noticeable after irradiation at temperatures between 400 and 580 °C and doses >20 dpa [12].

Non-equilibrium processes taking place under irradiation can also induce segregation and depletion of alloying elements at sinks (grain boundaries, dislocations, particle/matrix interphases, etc.), affecting the mechanical performance of these materials. These processes are called radiation-induced segregation (RIS) and radiation-induced depletion (RID). In particular, Cr segregation at grain boundaries could strengthen them as reported in Ref. [15], while depletion would enhance intergranular corrosion leading to fracture [16]. In irradiated austenitic steels, Cr is usually found to be depleted at sinks [17]. In the case of FM steels, both RIS and RID phenomena at grain boundaries have been reported after irradiation at different doses and temperatures. For example, Cr depletion was observed in the FM steel F82H after H^+ irradiation at 250 °C and doses as low as 0.5 dpa [15]. Cr enrichment was also reported for irradiation temperatures above 410 °C [17].

In this study, transmission electron microscopy (TEM) has been used to study the microstructural stability of an ODS Fe12Cr steel subjected to two different irradiation conditions: Fe ion irradiation at ~10 dpa and simultaneous Fe, He and H ion irradiation at ~4.4 dpa. Both irradiations were carried out at room temperature (RT). The simultaneous triple irradiation was carried out to investigate the effects of He and H on the steel. These transmutation gases will be generated from nuclear reactions in a fusion environment. The aim is to determine the irradiation-induced changes on the microstructure, such as the presence of loops and the effect on the grain boundary chemistry, oxide nanoparticles and other secondary phases present in this material.

Materials and methods

Materials

The ODS Fe12Cr steel (nominal composition Fe–12wt%Cr–0.4wt%Y_2O_3) was produced by mechanical alloying of elemental Fe and Cr powders and monoclinic Y_2O_3 nanopowders (<50 nm) followed by consolidation by hot isostatic pressing. The alloying process was carried out in an attritor mill at 300 rpm for 27 h under Ar atmosphere. After canning, degassing and sealing, the alloyed powder batches were subjected to HIP at 190 MPa and 1100 °C for 2 h. The consolidated batches were heat treated at 750 °C for 4 h [18]. A reference Fe12Cr steel identically processed was also studied to determine the impact of the nanoparticle dispersion on characteristics of radiation damage.

Irradiation parameters

The single (Fe^{4+}) and simultaneous triple (Fe^{8+}, He^+, H^+) irradiations were carried out at the Joint Accelerators for Nanosciences and Nuclear Simulation facility (JANNUS) at Saclay, Paris, France. The irradiations were performed at 20 °C. The irradiation conditions are presented in Table 1. The configuration of the single- and triple-beam chambers available at JANNUS-Saclay is described in Refs. [19–21]. For the single irradiation, the ion beam was perpendicular to the sample surface, while for the triple irradiation the incidence angles between the three ion beams and the axis perpendicular to the sample surface were 15°.

Irradiation doses were estimated using the binary collision Monte Carlo approximation formalism implemented in the SRIM2011 program [22]. The "full cascade" option

Journal : Large 10853 Dispatch : 18-12-2014 Pages : 12
Article No. : 8794 ☐ LE ☐ TYPESET
MS Code : JMSC-D-14-03261 ☑ CP

Table 1 Ion irradiation parameters

Irradiation	Temperature (°C)	Ion	Energy	Dose rate (ions/cm^2 s)	Fluence (ions/cm^2)
Single	(20 ± 1)	$^{56}Fe^{4+}$	10 MeV	4.6 × 10^{11}	5.0 × 10^{15}
Triple	(21 ± 1)	$^{56}Fe^{8+}$	24 MeV	1.2 × 10^{11}	2.2 × 10^{15}
		$^{4}He^{+}$	1.9 MeV	3.1 × 10^{11}	5.6 × 10^{15}
		$^{1}H^{+}$	600 keV	3.1 × 10^{11}	5.6 × 10^{15}

was used to simulate all collisional damage in an Fe–12Cr target. In this option, ions and recoiling atoms are individually followed until their energies drop below the displacement energy (minimum energy to displace an atom from its lattice site and create a stable Frenkel pair). The damage depth profiles for the two irradiation experiments performed are shown in Fig. 1. For the single irradiation, the Fe ion energy is 10 MeV with the maximum damage peak (Bragg peak) at ~2 μm, see Fig. 1a. The calculated dose at the peak was ~10 dpa. dpa values were calculated from Eq. 1 using displacement energies of 40 eV for Fe and Cr to estimate the number of vacancies (v) per ion and angstrom $\left(\frac{v}{\text{ion}\times\text{Å}}\right)$ from the SRIM program, following the ASTM standard E 521-96.

$$\text{dpa} = \left(\frac{v}{\text{ion}\times\text{Å}}\right)\times 10^{8}\left(\frac{\text{cm}}{\text{Å}}\right) \times \frac{\text{ion fluence (cm}^{-2})}{\text{sample atomic density (cm}^{-3})} \quad (1)$$

For the triple irradiation experiments, the ion energies were chosen (see Table 1) to produce a common Bragg peak at a depth of ~3 μm as shown in Fig. 1b. Unfortunately, in this irradiation experiment, the target damage of 10 dpa could not be achieved due to technical issues. The calculation using Eq. 1 yielded a maximum dose of ~4.4 dpa. The damage produced by the He and H ions was negligible and thus not considered for this estimation. The total dose of He and H implanted resulted in ~2000 appm at the Bragg peak for each ion, see Fig. 1b.

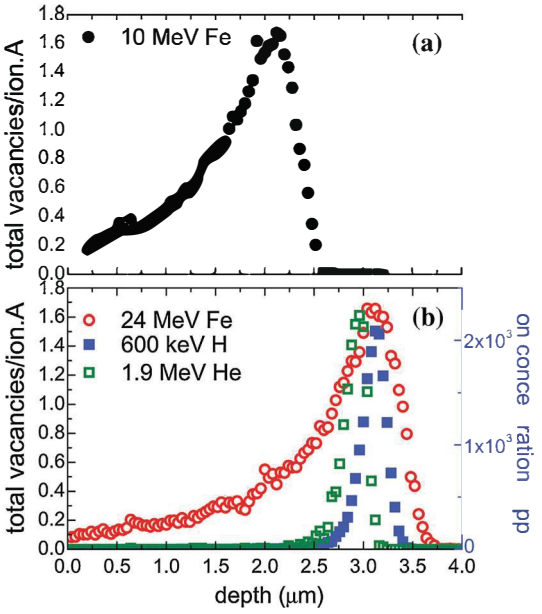

Fig. 1 SRIM damage profiles induced by **a** the single-beam irradiation with Fe ions of 10 MeV, and **b** the triple-beam irradiation with Fe ions of 24 MeV along with the implantation profiles corresponding to 1.9 MeV He and 600 keV H ions

TEM sample preparation and methods

Cross-sectional samples for TEM investigation were prepared in a Zeiss Auriga dual focused ion beam (FIB) operated at 30 kV using the lift-out technique [23]. A final milling at 5 keV was done to minimise the damage layer possibly induced by the FIB process. Illustrative examples of TEM samples obtained are presented in Fig. 2.

Analyses of the dislocation loops were accomplished in bright-field (BF) and diffraction modes using a Philips CM20 operated at 200 kV. The thicknesses t of the studied areas for determination of the loop number density were obtained from electron energy loss spectroscopy (EELS) spectra using the log-ratio method by means of the equation

$$t = \lambda \times \ln\left(\frac{I_t}{I_{ZLP}}\right), \quad (2)$$

where λ is the electron inelastic mean free path, I_t the total intensity of the EELS spectrum and I_{ZLP} the intensity of the zero loss peak [24].

This formula is valid for $t/\lambda \leq 4$. The t/λ values were <1.5 in all analysed areas. The inelastic mean free path λ

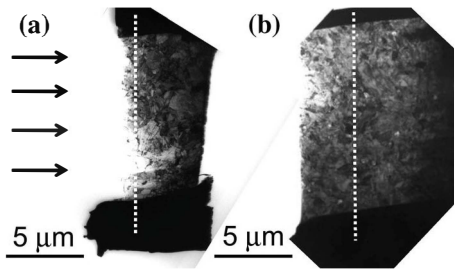

Fig. 2 Low-magnification BF-TEM images of the ODS Fe12Cr FIB samples after **a** the single- and **b** triple-ion-beam irradiations. The *dotted white line* marks the position of the Bragg peak

Journal : Large 10853 Dispatch : 18-12-2014 Pages : 12
Article No. : 8794 LE TYPESET
MS Code : JMSC-D-14-03261 CP

(in nm) was estimated in ~150 nm using the formula derived by Malis [25]

$$\lambda = \frac{106FE_o}{E_m \cdot \ln\left(2\beta E_o/E_m\right)} \quad (3)$$

In this equation, F is a relativistic correction factor defined by Eq. 4. E_o is the beam energy in keV (297 keV in this case), β is the collection angle and E_m is an average energy loss (in eV) that can be estimated as $E_m 7.5 \cdot Z_{ef}^{0.36}$, where Z_{ef} the effective atomic number.

$$F = \frac{1 + E_o/1022}{\left(1 + E_o/511\right)^2} \quad (4)$$

The grain boundary microchemistry was measured in scanning TEM (STEM) mode by performing EELS lines-cans on grain boundaries tilted to edge-on conditions. The chemical compositions of the secondary phases were also analysed by energy dispersive spectroscopy (EDS) and energy filtered TEM (EFTEM). EFTEM maps in the low-loss (10–100 eV) and core-loss (450–800 eV) energy ranges were acquired using 2 and 10 eV slits and steps of 2 and 10 eV, respectively. The collection semi-angle was 20 mrad. The EFTEM series were drift corrected and processed using multivariate statistical analysis (MSA) to maximise the signal-to-noise ratio [26, 27]. Backgrounds were fitted using an inverse power-law and subtracted applying a multi-windows technique as explained in Ref. [28]. TEM–EELS for thickness measurements as well as STEM-EDS and EFTEM maps were obtained with a JEOL 3000F TEM operated at 297 kV and equipped with a Gatan image filter (GIF).

Results and discussion

Unirradiated samples

Previous analyses of the unirradiated ODS and reference Fe12Cr steels under study have shown the following:

- After heat treatment, the grain structure consisted of recovered and recrystallised areas with grains exhibiting equiaxed morphologies and sub-micron sizes, and unrecovered areas where the high dislocation density prevented clear visualisation of the grain structure, especially in the ODS steel [29]. This inhomogeneous recovery appeared to be directly related to the inhomogeneous distribution of secondary phases, since recovery was achieved in areas depleted of Y- and Cr-rich particles.
- Cr enrichment was detected at some grain boundaries [30].
- Y-rich nanoparticles had sizes in the range ~1–40 nm. Number densities measured on unrecovered areas varied between $\sim 5 \times 10^{21}$ and 2×10^{22} m^{-3} in most of the analysed volumes. A few regions had densities of the order of 10^{23} m^{-3}. At least 40 % of the analysed particles corresponded to either monoclinic Y_2O_3 or $YCrO_3$. In certain particles, a structure consisting on an Y–O-rich core and a Cr-rich shell was evident [29].
- Other Cr-rich secondary phases with sizes between 50 nm and 1μm, mainly identified as $M_{23}C_6$ carbides and Cr_2O_3, were also present [29].
- Nano-voids are present in the studied samples, having sizes <5 nm for the ODS Fe12Cr steel [31]. This seems to be characteristic of steels milled under Ar atmosphere [31, 32].

Ion irradiated samples

General microstructure and irradiation-induced loops

No significant changes were evident in grain structures after the irradiations. However, small irradiation-induced dislocation loops were visible after the single and triple irradiations, see Fig. 3 and Ref. [33]. The loops were only clearly visible in the recovered/recrystallised areas of the samples, as the high dislocation density prevented their visualisation in unrecovered areas. In BF-TEM mode, these loops were viewed as small black dots clearly distinguishable by their contrast behaviour from the small nanoparticles present in the ODS steel. The loops exhibited in general a stronger contrast, and more sensitivity to diffraction conditions, than the particles. These loops were most clearly imaged under **g** {1 1 0} diffraction conditions, being **g** the reciprocal lattice vector.

To check if the observed loop features could also be due to small point defects induced by the sample preparation, a sample of the unirradiated ODS material was also prepared by FIB using identical conditions (see "TEM sample preparation and methods" section). No visible point defects were found under **g** {1 1 0} condition, see Fig. 4, indicating that the FIB process does not introduce visible point defects under these preparation conditions in these steels.

The loop sizes were estimated from the maximum dimension of the black dots. The relationship between the measured sizes and their true diameter depends on the depth of the loop in the foil, foil thickness and diffraction conditions; however, previous analyses have shown that this estimation may be accurate enough [34]. In any case, the aim of this study was to compare the relative sizes in the steels using the same methodology. The sizes of ~400 loops were measured in areas oriented along **g** {1 1 0}. Histograms depicting visible loop sizes for the single-ion-

Journal : Large 10853 Dispatch : 18-12-2014 Pages : 12
Article No. : 8794 LE TYPESET
MS Code : JMSC-D-14-03261 CP

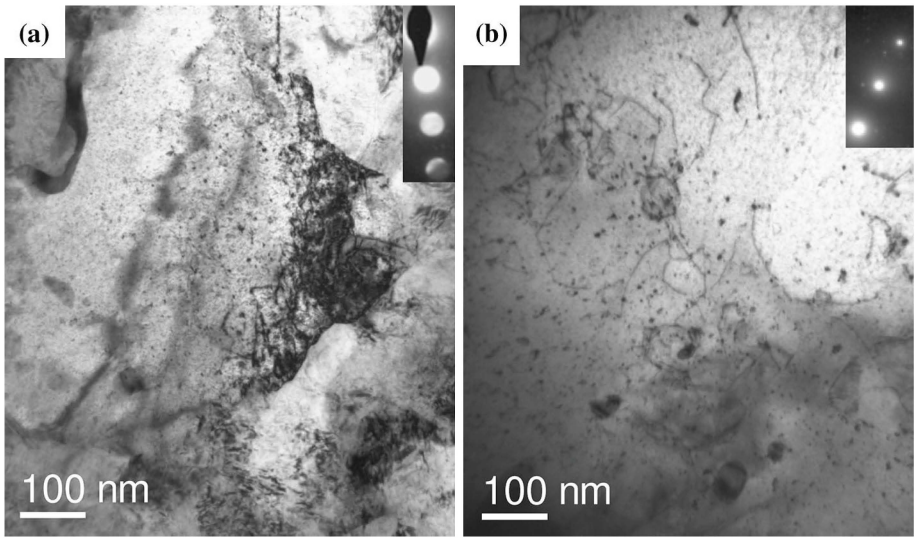

Fig. 3 BF images showing the loop distribution for **a** the single-ion-beam irradiated ODS Fe12Cr steel and **b** the non-ODS counterpart. The grains are oriented along **g** (1 1 0)

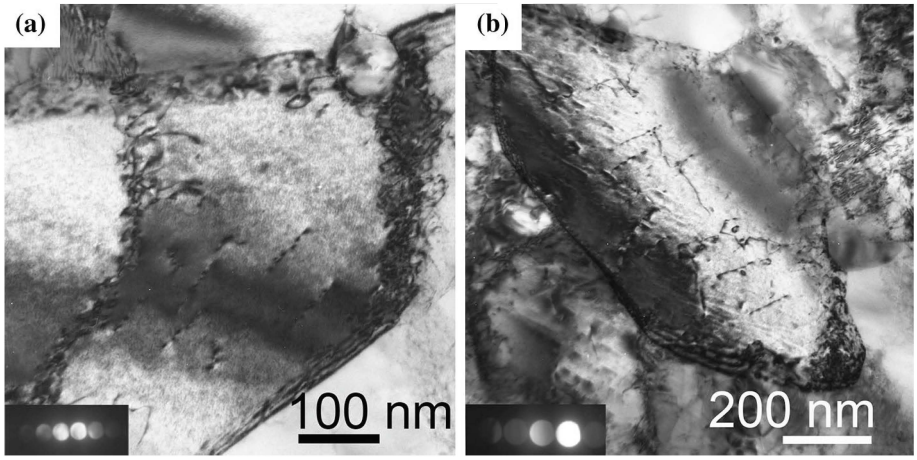

Fig. 4 BF images of the non-irradiated ODS-Fe12Cr steel. **a**, **b** show two different grains oriented along **g** {1 1 0}. Radiation damage loops are not observed

beam experiments are presented in Fig. 5. The size distribution width for the ODS steel is narrower and the sizes smaller. The mean loop diameter estimated from these measurements was 4 ± 2 nm for the ODS steel and 6 ± 3 nm for the non-ODS reference steel. These dimensions are smaller than the ones previously reported for the same ODS and non-ODS steels after Fe^{+} irradiation at 500 °C and ~7 dpa (10 ± 7 and 12 ± 10 nm, respectively) [35].

The size distribution of dislocation loops in the ODS steel after the triple irradiation is depicted in Fig. 5c. The size distribution for the triple-beam irradiated ODS steel is narrower with a mean loop size of 3 ± 1 nm, i.e. slightly smaller than the one for the single-beam irradiated counterpart. This is probably a result of the smaller dose achieved (4.4 dpa against 10 dpa for the single irradiated ODS steel).

Table 2 presents loop number densities for the single-beam irradiated ODS and non-ODS samples, measured in several grains ("Regions A–E") all oriented along **g** {1 1 0}. The number densities are of the same order of magnitude, i.e. $\sim 10^{22}$ m^{-3}. In particular, the number densities measured for the ODS sample in regions A and B closely match the ones obtained in region D for the non-ODS sample. The densities measured for the non-ODS sample in regions C and E appear to be slightly lower but this is very likely due to the fact that the volumes of study for these regions were larger (i.e. the resolution was lower) so the measurements may be slightly skewed. Overall, the dislocation loop number densities are very similar for the ODS and non-ODS variants of the steels. However, it has to be taken into account that densities had to be measured on recovered areas in the ODS steel, which are dislocation free but have a lower density of nanoparticles. This might bias the results. Indeed, recent in situ Fe^{+} irradiations performed on PM2000 foils to doses of ~1.5 dpa showed that the number density of defects present in the matrix decreases with increasing particle number density [36].

Journal : Large 10853 Dispatch : 18-12-2014 Pages : 12
Article No. : 8794 LE TYPESET
MS Code : JMSC-D-14-03261 CP

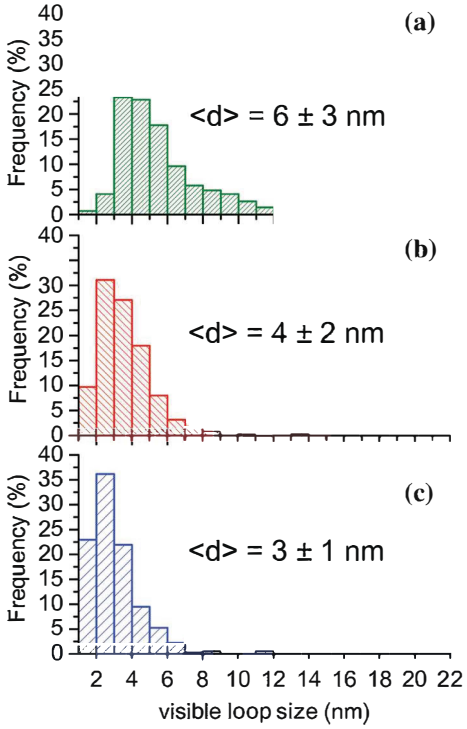

Fig. 5 Histograms showing the loop size distributions for single-ion-beam irradiated **a** non-ODS Fe12Cr and **b** ODS Fe12Cr steels. **c** Loop size distribution for the triple-ion-beam irradiated ODS Fe12Cr steel. These distributions might be skewed due to the low visibility of loops of sizes less than ~2 nm and the resolution limit of the microscope

The presence of irradiation-induced bubbles in the triple-ion irradiated steel was also investigated. The single- and triple-ion-beam irradiated steels exhibited small features having contrasts corresponding to voids or bubbles, with sizes similar to those found for the unirradiated steel (<5 nm). Consequently, it cannot be assured that they are irradiation-induced, as reported in Ref. [33].

Grain boundary chemistry after irradiation

In unirradiated FM steels, Cr segregation at grain boundaries due to thermal diffusion is usually detected after annealing [15]. This is the case for the ODS-Fe12Cr steel under study (see "Unirradiated samples" section). Cr RIS and RID have both been reported in irradiated FM steels as outlined in "Introduction" section; both RIS and RID have been observed in grain boundaries of samples of the present ODS 12FeCr steel Fe^{+} irradiated at 500 °C [30]. Whether RIS or RID occurs may be related to grain boundary sink strength. For austenitic and more recently for ferritic steels, it was shown that high-angle boundaries are much more efficient defect sinks than low-angle boundaries [37, 38]. In principle, these phenomena are expected to happen at temperatures between ~0.2 and 0.7 times the melting temperature of the alloy, also depending on the dose rate as reported in [16]. However, RIS was reported after RT irradiation in a 304 austenitic stainless steel [39]. In order to check if the RIS and RID phenomena are concurrent in the ODS Fe12Cr steel irradiated in this study, EELS analyses were performed. For each sample, ten boundaries located near the Bragg peak were analysed by performing EELS linescans in the core-loss region where only the Cr $L_{2,3}$, O K and Fe $L_{2,3}$ edges would be visible, i.e. over the energy loss range 400–800 eV.

Examples are shown in Fig. 6. For the single-beam irradiated ODS Fe12Cr steel samples, ~30 % of the analysed boundaries were clearly enriched in Cr, which is a similar behaviour to that found in the unirradiated counterpart sample. No Cr depletion at grain boundaries appears to occur in these samples. In the case of the triple-beam irradiated samples, the behaviour was similar to those single-beam irradiated, with ~20 % of the analysed grain boundaries enriched in Cr, and no Cr-depleted boundaries observed.

Stability of secondary phases after irradiation

Y-rich nanoparticles The irradiation-induced evolution of the nanoparticles present in ODS steels has been investigated by atom probe tomography (APT) [12, 13, 40] and by TEM studies, mostly performed using conventional BF/DF-TEM techniques [8, 12, 41–43]. However, due to the variety of features giving diffraction contrast in the BF

Table 2 Visible loop densities measured for the ODS and reference single-ion irradiated steels in regions located at a depth of ~2 μm from the irradiated surface (i.e. at the maximum damage peak)

ODS/Fe12Cr	Volume ($\times 10^{-20}$ m^3)	Visible loop density g {110} ($\times 10^{21}$ m^{-3})
Region A	0.6 ± 0.1	17 ± 3
Region B	0.5 ± 0.1	22 ± 4
Fe12Cr	Volume ($\times 10^{-20}$ m^3)	Visible loop density g {110} ($\times 10^{21}$ m^{-3})
Region C	9 ± 2	8 ± 2
Region D	1.2 ± 0.2	16 ± 3
Region E	3.8 ± 0.8	10 ± 2

Journal : Large 10853 Dispatch : 18-12-2014 Pages : 12
Article No. : 8794 ☐ LE ☐ TYPESET
MS Code : JMSC-D-14-03261 ✓ CP

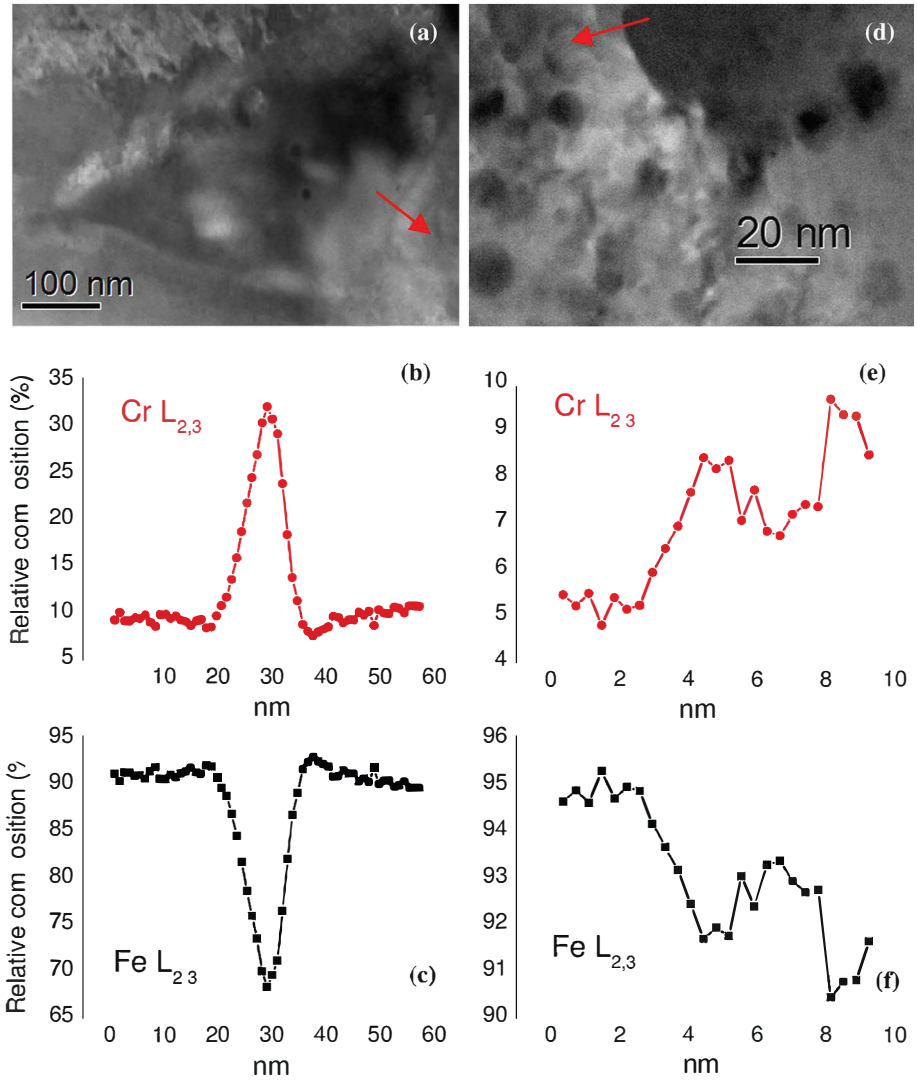

Fig. 6 **a** High-angle annular dark-field (HAADF)-STEM image of the single-ion-beam irradiated ODS Fe12Cr steel. **b**, **c** are Cr and Fe EELS linescans across the grain boundary marked on (**a**). **d** HAADF-STEM image of the triple-ion-beam irradiated ODS Fe12Cr steel. **e**, **f** are Cr and Fe EELS linescans across the grain boundary marked on (**d**)

images of the irradiated ODS steels, it is advisable to analyse the secondary phase distribution using analytical techniques such as EFTEM or STEM combined with EELS or EDS. These methods minimise diffraction contrast and in combination provide the information needed to investigate the chemical evolution of the particles after irradiation. Only very few reports have been found that apply these advanced techniques to accomplish such analyses [13, 28, 44]. Some authors use Fe EFTEM maps to visualise the nanoparticles and APT to study their chemical evolution because attaining reliable Y EFTEM maps is a challenging task due to the locations of its three electron energy loss edges [13, 44]. For instance, the Y $L_{2,3}$ edge with its onset at 2085 eV is out of the range that can be acquired, and the Y $M_{2,3}$ edge (onset at 156 eV) provides a weaker signal than the Y $N_{2,3}$ edge (onset at 26 eV), besides overlapping with the plasmon peak. The method used here (see "TEM sample preparation and methods" section) allows obtaining Y-$N_{2,3}$ maps capable of resolving nanoparticles of just a few nm in diameter (~4 nm in the samples used in this work).

Figures 7, 8 and 9 depict STEM-EDS and EFTEM maps showing the Cr-rich and Y-rich secondary phases in the ODS steel after the single-beam (10 dpa) and triple-beam (4.4 dpa) irradiations. The Y-rich particles are heterogeneously distributed as shown in Fig. 7. Particle number densities ranged between $\sim 1 \times 10^{21}$ and 2×10^{22} m^{-3} after both irradiations. These densities are similar to those found in the unirradiated samples (see "Unirradiated samples" section). The particle size distributions found for the irradiated and non-irradiated ODS steels are depicted in Fig. 10. These histograms were obtained by measuring more than 300 particles in each specimen type. The mean particle sizes of the three distributions are similar. A slight

Journal : Large 10853 Dispatch : 18-12-2014 Pages : 12
Article No. : 8794 LE TYPESET
MS Code : JMSC-D-14-03261 CP

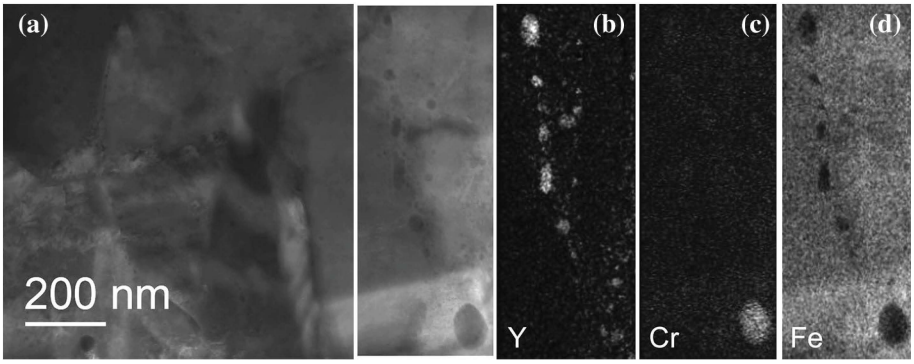

Fig. 7 **a** HAADF-STEM image showing the particle dispersion in the single-ion-beam irradiated ODS Fe12Cr steel. The marked area is the region selected for mapping. **b** Y (L + M), **c** Cr L and **d** Fe L EDS maps showing Y-rich nanoparticles and a Cr-rich precipitate in this region

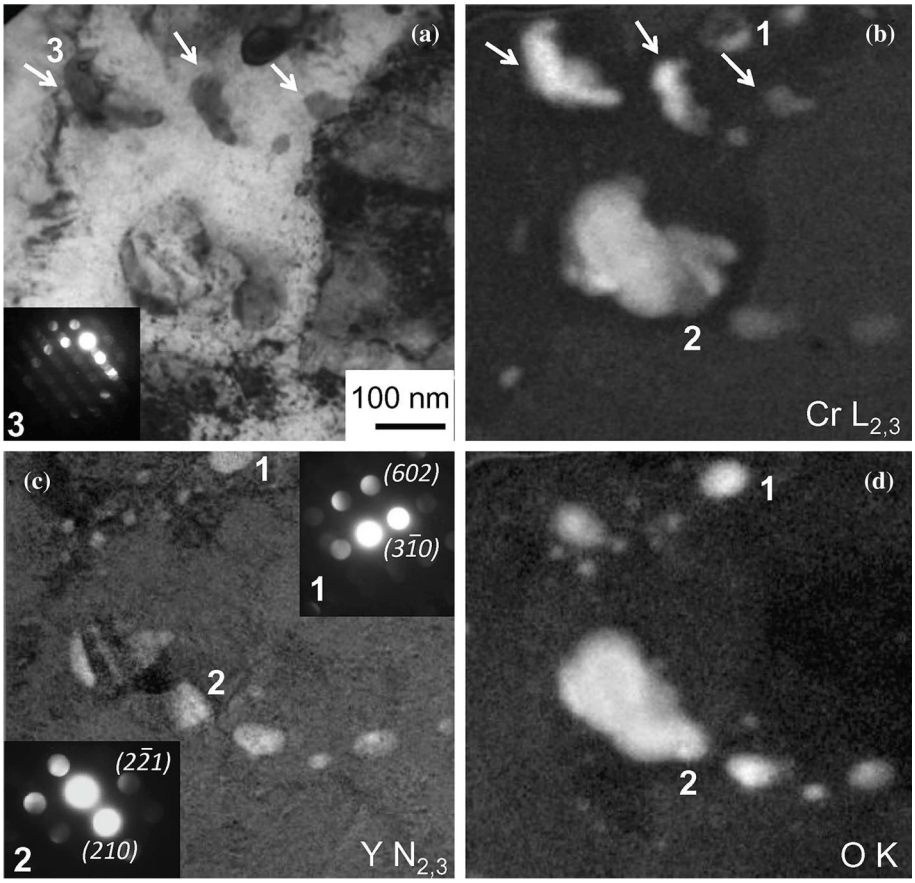

Fig. 8 **a** BF image and **b–d** Cr, Y and O EFTEM maps showing the secondary phases present on the single-ion-beam irradiated ODS Fe12Cr steel. The *insets* show the microdiffraction patterns of particles marked as 1, 2 and 3. Particle 1 is identified as monoclinic Y_2O_3 oriented along the $[1\ \ 3\ \ \bar{3}]$ zone axis and particle 2 as $YCrO_3$ oriented along the $[\bar{1}\ \ 2\ \ 6]$ zone axis (indexation errors <10 %). Some diffraction spots are indexed for clarification. Precipitate 3 is identified as $M_{23}C_6$ (M = Cr, Fe) oriented along the [1 2 3] zone axis. The Cr-rich precipitates marked with *arrows* do not contain O

tendency to smaller particle sizes is apparent for the single-beam irradiated ODS sample; this underwent the higher irradiation dose (~10 dpa).

No differences in particle composition were evident after the single- or triple-beam irradiations. Two chemical compositions, Y–O and Y–Cr–O, are detected (see Figs. 7, 8, 9). These are the same compositions found in the unirradiated ODS samples ("Unirradiated samples" section). A Cr-rich shell was visible in some of the Y–O particles after the irradiations. To detect this core–shell structure, EELS linescans were performed across 20 nanoparticles for each of the irradiation conditions. For the single-beam irradiated ODS samples, 20 % of the nanoparticles presented a core–shell structure with clear Cr depletion in the core, and the others exhibited a uniform distribution of Y and Cr (see Fig. 11a, b). For the triple-beam irradiated ODS steel, 35 % of the studied nanoparticles presented a core–shell structure (see Fig. 11c).

Journal : Large 10853 Dispatch : 18-12-2014 Pages : 12
Article No. : 8794 ☐ LE ☐ TYPESET
MS Code : JMSC-D-14-03261 ☑ CP

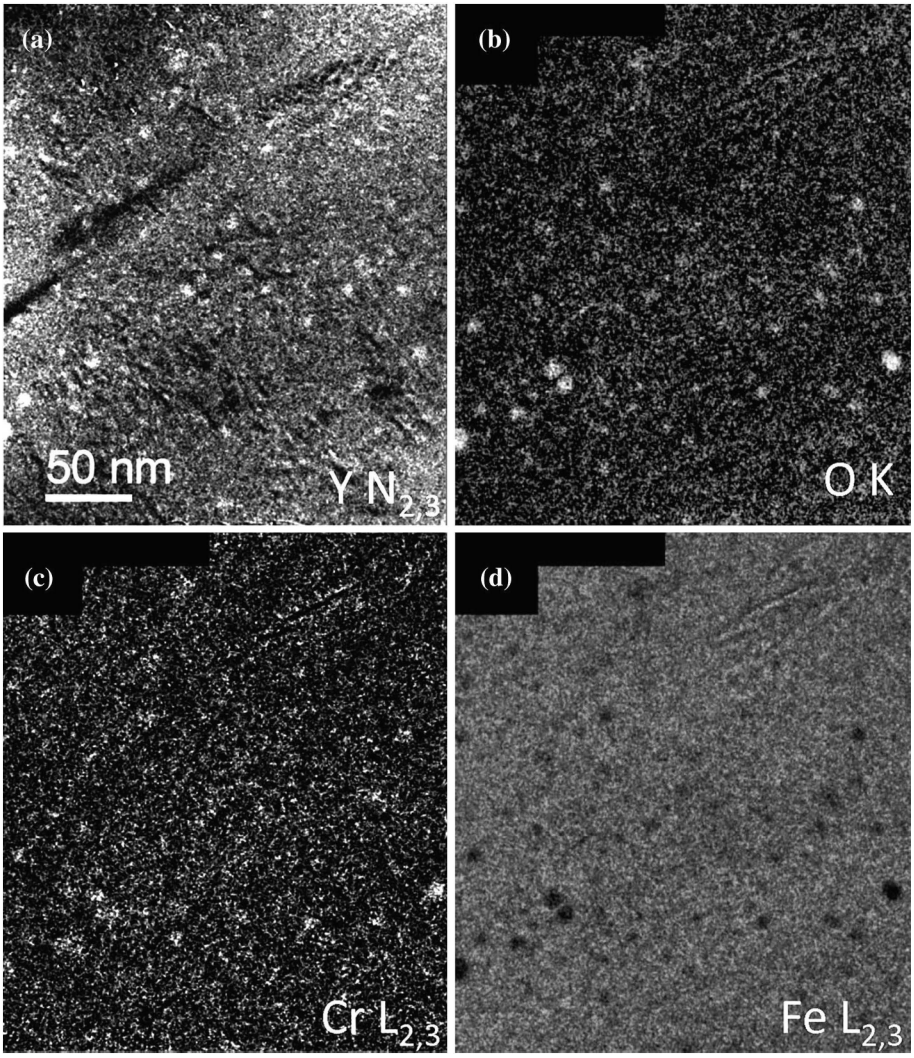

Fig. 9 EFTEM series showing the chemical composition of the nanoparticles in the triple-ion-beam irradiated ODS Fe12Cr steel. **a** Y $N_{2,3}$, **b** O K, **c** Cr $L_{2,3}$, **d** Fe $L_{2,3}$ elemental maps

High-resolution electron microscopy (HREM) measurements could not be properly accomplished due to sample degradation. Nevertheless, the crystal structures of several large nanoparticles (~60 nm) were investigated by microdiffraction in the single-beam irradiated samples. The microdiffraction patterns shown as insets in Fig. 8c are from the particles marked as 1 and 2 in the corresponding EFTEM maps. EFTEM analyses reveal that particle 1 has a Y–O-rich core surrounded by a Cr-rich region. This particle was identified from its diffraction pattern as monoclinic Y_2O_3 (indexation error: 7 %). Particle 2, having a homogeneous Y–Cr–O composition, was identified as $YCrO_3$ (indexation error: 8 %).

Cr-rich precipitates The stability of the larger Cr-rich precipitates present in the ODS and non-ODS samples was also investigated. The two Cr-rich phases clearly identified in the non-irradiated steels are Cr_2O_3 and $M_{23}C_6$ (M = Cr, Fe). The phases present after irradiation appear to be similar (see example in Fig. 8). However, some Cr-rich precipitates having less well-defined morphologies were detected in the single-beam irradiated ODS sample as shown in Fig. 8. The three Cr-rich precipitates marked with arrows in the figure do not contain oxygen. It can be concluded that they are Cr carbides. This assumption is also supported by the fact that one of the analysed precipitates was indexed as $M_{23}C_6$ (inset in Fig. 8a). These observations suggest that $M_{23}C_6$ carbides could evolve under the present irradiation conditions. $M_{23}C_6$ partial dissolution, coarsening, modification of chemical composition and amorphization phenomena have previously been observed in several Fe-(9–12)wt% Cr steels ion and neutron irradiated under different doses (in the range 2–50 dpa) and temperatures (RT to 600 °C) [45–48].

Journal : Large 10853 Dispatch : 18-12-2014 Pages : 12
Article No. : 8794 LE TYPESET
MS Code : JMSC-D-14-03261 CP

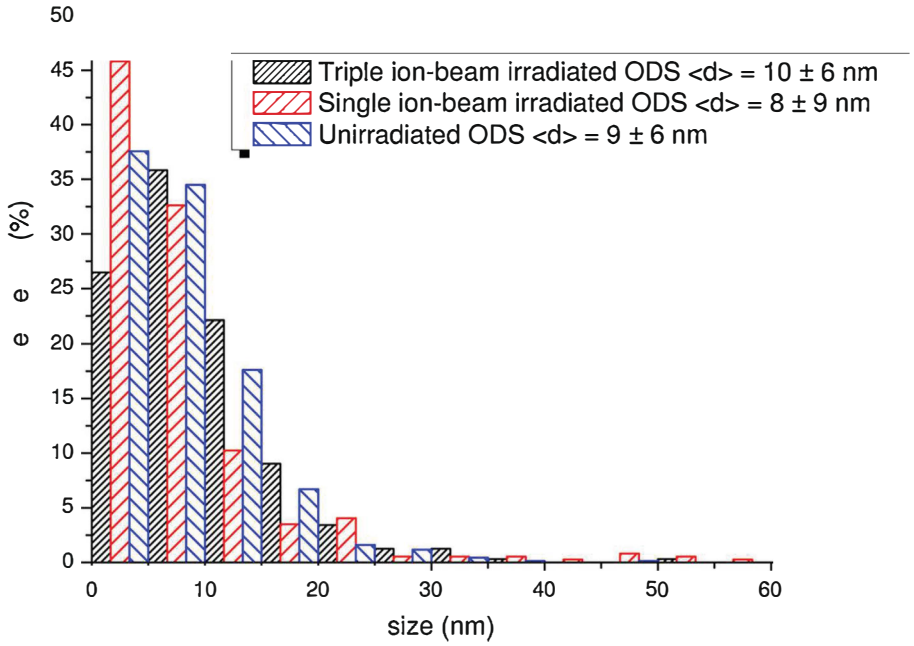

Fig. 10 Histogram depicting the nanoparticle size distributions in the unirradiated, single- and triple-ion-beam irradiated ODS Fe12Cr steels

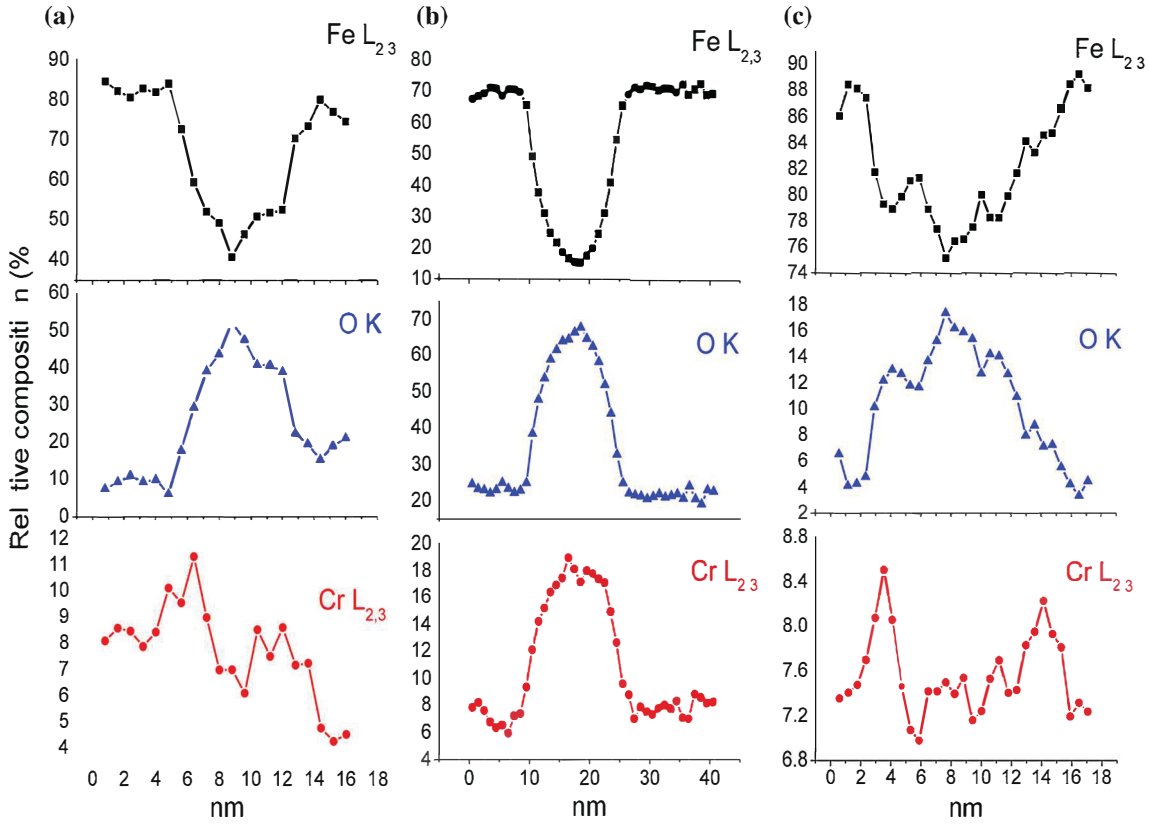

Fig. 11 Cr, O and Fe EELS linescans across Y-rich nanoparticles showing: **a** Cr-rich shell in the single-ion irradiated ODS steel, **b** homogeneous Y–Cr–O nanoparticle in the single-ion-beam irradiated ODS steel, **c** Cr-rich shell in the triple-ion-beam irradiated ODS steel

Journal : Large 10853 Dispatch : 18-12-2014 Pages : 12
Article No. : 8794 LE TYPESET
MS Code : JMSC-D-14-03261 CP

Conclusions

Ion irradiation experiments at 20 °C using single beam with Fe ions (10 dpa), and simultaneous triple beam with Fe + He + H ions (4.4 dpa, 2000 appm H, 2000 appm He) were performed on an ODS Fe12Cr steel and its non-ODS counterpart. The main conclusions of this study are the following:

(1) Irradiation-induced loops, observed as small black dots in the TEM images, are present in all three materials after both irradiation types. Loop sizes measured for the irradiated ODS steel appear to increase with dose. The sizes are smaller compared with the single-beam irradiated reference material. No significant changes are found in the number densities ($\sim 10^{22}$ m^{-3}) when comparing the reference and ODS single-beam irradiated steels.

(2) The triple-ion-beam irradiated ODS steel exhibited features with contrasts corresponding to small nano-voids or bubbles (<5 nm). Similar features are also found on the counterpart unirradiated steel. Consequently, it cannot be assured that they are induced by the irradiation.

(3) Cr enrichment at ~20–30 % of grain boundaries is observed after the single- or triple-beam irradiation experiments. This behaviour is akin to the one found for the non-irradiated ODS steel [28].

(4) No significant changes in the sizes, morphology and composition of the Y-rich particles are found after the single or triple irradiations compared to those in the non-irradiated samples.

(5) The $M_{23}C_6$ carbides in these steels could have evolved during irradiation at the higher dose (10 dpa), possibly by partially dissolution and re-precipitation.

Acknowledgements This investigation was supported by the Ministerio de Ciencia e Innovación (Contract ENE2010-17462), the European Commission through the European Fusion Development Agreement (EFDA), the EPSRC Grant No. EP/H018921/1, the FP7-EU Program under Grant Agreement 312483 - ESTEEM2 (Integrated Infrastructure Initiative-I3) and the Royal Society International Exchanges Scheme 2011/R1 (ref. IE110136).

References

1. Boutard JL, Alamo A, Lindau R, Rieth M (2008) Fissile core and tritium-breeding blanket: structural materials and their requirements. C R Phys 9:287–302
2. Ukai S, Fujiwara M (2002) Perspective of ODS alloys application in nuclear environments. J Nucl Mater 307–311:749–757
3. Odette GR, Alinger MJ, Wirth BD (2008) Recent developments in irradiation-resistant steels. Annu Rev Mater Res 38:471–503
4. Ramar A, Schäublin R (2013) Analysis of hardening limits of oxide dispersion strengthened steel. J Nucl Mater 432:323–333
5. Schäublin R, Ramar A, Baluc N, de Castro V, Monge MA, Leguey T, Schmid N, Bonjour C (2006) Microstructural development under irradiation in European ODS ferritic/martensitic steels. J Nucl Mater 351:247–260
6. Kishimoto H, Yutani K, Kasada R, Kimura A (2006) Helium cavity formation research on oxide dispersed strengthening (ODS) ferritic steels utilizing dual-ion irradiation facility. Fus Eng Des 81:1045–1049
7. Hsiung LL, Fluss MJ, Tumey SJ, Choi BW, Serruys Y, Willaime F, Fimura A (2010) Phys Rev B 82:184103
8. Ramar A, Baluc N, Schaüblin R (2007) Effect of irradiation on the microstructure and the mechanical properties of oxide dispersion strengthened low activation ferritic/martensitic steel. J Nucl Mater 367–370:217–221
9. Robertson C, Panigrahi BK, Balaji S, Kataria S, Serruys Y, Mathon MH, Sundar CS (2012) Particle stability in model ODS steel irradiated up to 100 dpa at 600 C: TEM and nano-indentation investigation. J Nucl Mater 426:240–246
10. Ukai S (2012) Oxide dispersion strengthened steels. Comp Nucl Mater 4:241–271
11. Lescoat ML, Ribis J, Gentils A, Kaïtasov O, de Carlan Y, Legris A (2012) In situ TEM study of the stability of nano-oxides in ODS steels under ion-irradiation. J Nucl Mater 428:176–182
12. Allen T, Gan J, Cole JI, Miller MK, Busby JT, Shutthanandan S, Thevuthasan S (2008) Radiation response of a 9 chromium oxide dispersion strengthened steel to heavy ion irradiation. J Nucl Mater 375:26–37
13. Certain A, Kuchibhatla S, Shutthanandan V, Hoelzer DT, Allen TR (2013) Radiation stability of nanoclusters in nano-structured oxide dispersion strengthened (ODS) steels. J Nucl Mater 434:311–321
14. Akasaka N, Yamashita S, Yoshitake T, Ukai S, Kimura A (2004) Microstructural changes of neutron irradiated ODS ferritic and martensitic steels. J Nucl Mater 329–333:1053–1056
15. Schaüblin R, Spätig P, Victoria M (1998) Chemical segregation behavior of the low activation ferritic/martensitic steel F82H. J Nucl Mater 258–263:1350–1355
16. Nastar M, Soisson F (2012) Radiation-induced segregation. Comp Nucl Mater 1:471–496
17. Lu Z, Faulkner R, Was G, Wirth BD (2008) Irradiation-induced grain boundary chromium microchemistry in high alloy ferritic steels. Scripta Mater 58:878–881
18. de Castro V, Leguey T, Muñoz A, Monge MA, Pareja R, Marquis EA, Lozano-Perez S, Jenkins ML (2009) Microstructural characterization of Y_2O_3 ODS–Fe–Cr model alloys. J Nucl Mater 386–388:449–452
19. Serruys Y, Trocellier P, Miro S, Bordas E et al (2009) JANNUS: a multi-irradiation platform for experimental validation at the scale of the atomistic modelling. J Nucl Mater 386–388:967–970
20. Pellegrino S, Trocellier P, Miro S, Serruys Y et al (2012) The JANNUS Saclay facility: a new platform for materials irradiation, implantation and ion beam analysis. Nucl Instr Method B 273:213–217
21. Trocellier P, Miro S, Serruys Y, Vaubaillon S, Pellegrino S, Agarwal S, Moll S, Beck L (2014) Study of helium migration in nuclear materials at Jannus-Saclay. Nucl Instrum Methods Phys Res B 331:55–64
22. Ziegler J, Biersack J, Littmark U (1993) The stopping and power and range of ions in solids. Pergamon Press, New York
23. Lozano-Perez S (2008) A guide on FIB preparation of samples containing stress corrosion crack tips for TEM and atom-probe analysis. Micron 39:320–328

Journal : Large 10853 Dispatch : 18-12-2014 Pages : 12
Article No. : 8794 ☐ LE ☐ TYPESET
MS Code : JMSC-D-14-03261 ☑ CP

24. Williams DB, Carter CB (2009) High energy-loss spectra and images. Transmission electron microscopy: a textbook for materials science. Springer, Berlin, pp 715–739
25. Malis T, Cheng SC, Egerton RF (1998) EELS Log-Ratio Technique for Specimen-Thickness Measurement in the TEM. J Electron Microsc Tech 8:193–200
26. Schaffer B, Grogger W, Kothleitner G (2004) Automated spatial drift correction for EFTEM image series. Ultramicroscopy 102:27–36
27. Trebbia P, Bonnet N (1990) EELS elemental mapping with unconventional methods I. Theoretical basis. Image analysis with multivariate statistics and entropy concepts. Ultramicroscopy 34:165–178
28. Lozano-Perez S, de Castro Bernal V, Nicholls RJ (2009) Achieving sub-nanometre particle mapping with energy-filtered TEM. Ultramicroscopy 109:1217–1228
29. de Castro V, Marquis EA, Lozano-Perez S, Pareja R, Jenkins ML (2011) Stability of nanoscale secondary phases in an oxide dispersion strengthened Fe–12Cr alloy. Acta Mater 59:3927–3936
30. Marquis EA, Lozano-Perez S, de Castro V (2011) Effects of heavy-ion irradiation on the grain boundary chemistry of an oxide-dispersion strengthened Fe–12 wt% Cr alloy. J Nucl Mater 417:257–261
31. de Castro V, Lozano-Perez S, Marquis EA, Auger MA, Leguey T, Pareja R (2011) Analytical characterisation of oxide dispersion strengthened steels for fusion reactors. Mater Sci Tech 27:719–723
32. Klimiankou M, Lindau R, Möslang A (2005) Energy-filtered TEM imaging and EELS study of ODS particles and Argon-filled cavities in ferritic–martensitic steels. Micron 36:1–8
33. de Castro V, Briceno M, Lozano-Perez S, Trocellier P, Roberts SG, Pareja R (2014) TEM characterization of simultaneous triple ion implanted ODS Fe12Cr. J Nucl Mater 455:157–161
34. Jenkins ML, Kirk MA (2001) Analysis of small centres of strain: counting and sizing small clusters. Characterization of radiation damage by transmission electron microscopy. Bristol, Institute of Physics, pp 110–128
35. de Castro V, Lozano-Perez S, Marquis EA, Jenkins ML (2009) Microstructural characterization of self ion irradiated ODS and Fe-Cr alloys presented at TMS2009 conference
36. de Castro V, Briceno M, Jenkins ML, Kirk M, Lozano-Perez S, Roberts SG (2014) In-situ Fe^{+} ion irradiation of an oxide dispersion strengthened steel. J Phys 522:012032
37. Watanabe S, Takamatsu Y, Sakaguchi N, Takahashi H (2000) Sink efect of grain boundary on radiation-induced segregation in austenitic stainless steel. J Nucl Mater 283–287:152–156
38. Hu R, Smith GDW, Marquis EA (2013) Effect of grain boundary orientation on radiation-induced segregation in a Fe–15.2 at.% Cr alloy. Acta Mater 61:3490–3498
39. Kawatsura K, Nakae T, Takahashi R, Nakai Y et al (1996) Analysis of radiation-induced segregation in type 304 stainless steel by PIXE and RBS channeling. Nucl Instr and Meth B 118:363–366
40. Pareige P, Miller MK, Stoller RE, Hoelzer DT, Cadel E, Radiguet B (2007) Stability of nanometer-sized oxide clusters in mechanically-alloyed steel under ion-induced displacement cascade damage conditions. J Nucl Mater 360:136–142
41. Kishimoto H, Yutani K, Kasada R, Hashitomi O, Kimura A (2007) Heavy-ion irradiation effects on the morphology of complex oxide particles in oxide dispersion strengthened ferritic steels. J Nucl Mater 367–370:179–184
42. Yamashita S, Yano Y, Ohtsuka S, Yoshitake T, Kaito T, Koyama S, Tanaka T (2013) Irradiation behavior evaluation of oxide dispersion strengthened ferritic steel cladding tubes irradiated in JOYO. J Nucl Mater 442:417–424
43. Liu C, Yu C, Hashimoto N, Ohnuki S, Ando M, Shiba K, Jitsukawa S (2011) Micro-structure and micro-hardness of ODS steels after ion irradiation. J Nucl Mater 417:270–273
44. Bentley J, Hoelzer DT, Busby JT, Certain AG, Allen TR, Kaoumi D, Motta AT, Kirk MA (2009) TEM characterization of crept and irradiated nano-structured ferritic alloys. Microsc Microanal 15(S2):1350
45. Klueh RL, Harries DR (2001) Interfacial segregation and precipitation during irradiation. High-chromium ferritic and martensitic steels for nuclear applications. ASTM, Bridgeport, pp 103–112
46. Tanigawa H, Sakasegawa H, Klueh RL (2005) Irradiation effects on precipitation in reduced-activation ferritic/martensitic steels. Mater Trans 46–3:469–474
47. Jin SX, Guo LP, Yang Z, Fu DJ et al (2011) Microstructural evolution of P92 ferritic/martensitic steel under argon ion irradiation. Mater Charact 62:136–142
48. Jia X, Dai Y, Victoria M (2002) The impact of irradiation temperature on the microstructure of F82H martensitic/ferritic steel irradiated in a proton and neutron mixed spectrum. J Nucl Mater 305:1–7

Journal : Large 10853 Dispatch : 18-12-2014 Pages : 12
Article No. : 8794 ☐ LE ☐ TYPESET
MS Code : JMSC-D-14-03261 ☑ CP